Separation of Subcutaneous Fat From Muscle in Surface Electrical Impedance Myography Measurements Using Model Component Analysis

Hyeuknam Kwon, Wasim Q. Malik, *Senior Member, IEEE*, Seward B. Rutkove, *Member, IEEE*, and Benjamin Sanchez, *Member, IEEE*

***Abstract*—*Objective*: Electrical impedance myography (EIM) is a relatively new technique to assess neuromuscular disorders (NMD). Although the application of EIM using surface electrodes (sEIM) has been adopted by the neurology community in recent years to evaluate NMD status, sEIM's sensitivity as a biomarker of skeletal muscle condition is impacted by subcutaneous fat (SF) tissue. Here, we develop a method that is able to remove the contribution of SF from sEIM data. *Methods*: We evaluate independent component analysis (ICA) and principal component analysis (PCA) for this purpose. Then, we introduce the so-called model component analysis (MCA). All methods are validated with numerical simulations using impedivity data from SF and muscle tissues. The methods are then tested with measurements performed in diseased individuals ($n = 3$). *Results*: Simulations demonstrate that MCA is the most accurate method at separating the impedivity of SF and muscle tissues with the accuracy being 99.2%, followed by ICA with 51.4%, and finally PCA with 38.5%. Experimental results from sEIM data measured on the triceps brachii of patients are consistent with muscle grayscale level values obtained using ultrasound imaging. *Conclusion*: MCA can be used to separate the impedivity of SF and muscle tissues from sEIM data, thus increasing the sensitivity to detect changes in the muscle. *Significance*: MCA can make the sEIM technique a better diagnostic tool and biomarker of disease progression and response to therapy by removing the confounding effect of SF tissue in NMD patients with excess subcutaneous fat tissue for any reason.**

***Index Terms*—Electrical impedance myography (EIM), model component analysis (MCA), independent component analysis (ICA), principal component analysis (PCA).**

Manuscript received March 9, 2018; revised May 7, 2018; accepted May 19, 2018. Date of publication May 23, 2018; date of current version January 18, 2019. This research was supported by grant NIH/NINDS 2K24NS060951 to Dr. Rutkove. Dr. Malik thanks the Craig H. Neilsen Foundation, Michael J. Fox Foundation, Morton Cure Paralysis Fund, and Huntington's Disease Society of America. *(Corresponding author: Benjamin Sanchez.)*

W. Q. Malik is with the Department of Anesthesia, Critical Care and Pain Medicine, Massachusetts General Hospital, Harvard Medical School.

H. Kwon, S. B. Rutkove, and B. Sanchez are with the Department of Neurology, Division of Neuromuscular Diseases, Beth Israel Deaconess Medical Center, Harvard Medical School, Boston, MA 02215-5491 USA (e-mail: bsanchez@bidmc.harvard.edu).

Digital Object Identifier 10.1109/TBME.2018.2839977

I. Introduction

ELECTRICAL impedance myography (EIM) is a specific instance of the broader electrical bioimpedance field [1], in which an electrical current is applied to an individual muscle or group of muscles and the generated voltages are measured. Over the last decades, studies have shown that EIM can serve as a painless biomarker to evaluate muscle health in patients with neuromuscular disorders (NMD) [2], including amyotrophic lateral sclerosis [3], [4] and Duchenne muscular dystrophy (DMD) [5], [6] as well in patients with muscle atrophy due to disuse or aging [7]. EIM has the potential of fulfilling a variety of valuable roles, including: 1. Assisting with primary diagnostic classification (e.g., primary myopathic versus neuropathic disease) [8]; 2. Assisting with tracking disease progression and response to therapy (i.e., serving a biomarker for clinical trials research) [9] and 3. Serving as a convenient marker for assisting physical therapists in modifying therapies during rehabilitation from primary musculoskeletal injury [10]. Simply put, EIM data provides easily obtained and actionable indices for a wide variety of disorders affecting skeletal muscle.

Although there have been an increasing number of studies employing EIM over the last 2 decades, there are still major technical challenges to its successful application that remain to be solved. For example, while the standard approach to applying EIM using surface electrodes (sEIM) offers the advantages of being non-invasive and rapid to perform, sEIM's sensitivity as a biomarker of NMD progression and response to therapy is reduced by subcutaneous fat (SF) tissue overlying the muscles [11]. To overcome the impact of SF tissue on sEIM data, previous studies have divided sEIM values measured at two different frequencies. The trial and error process for determining these two frequencies consists of correlating the result of the division with SF thickness at each and every one of the measured frequencies and choosing the combination with the least correlation [12]–[14]. However, there is no clear rationale for why such an approach should improve the contribution of the muscle to the outcome. Moreover, the outcome has no physiological meaning for the muscle.

In fact, one can understand this goal of separating the contribution of SF from muscle tissue in sEIM as one type of

source separation (SS) problem in which the electrical impedivity property of both tissues (henceforth the source signals) are "mixed" together in the sEIM data (the observed signals). The field of SS emerged in the 1950s and, since then, it has received increasing attention. In general terms, SS methods assume a statistical model whereby the observed signals are the result of a (non)linear combination of some (un)known source signals. In life science applications, for example, SS methods have found their niche for either removing interfering signals or separating signals that originated from temporally correlated and spatially distributed signals.

In particular, blind SS (BSS) corresponds to the specific case when the parameter values of the mixing model are considered unknown. Among the BSS techniques available, perhaps the most well-known techniques are the independent component analysis (ICA) [15], in which the source signals are assumed to be nongaussian and mutually independent, and the principal component analysis (PCA) [16], where independence is forced onto the data through an orthogonal transformation. In contrast, in the nonblind case, prior information about the source signals is available so that it can be introduced into the model [17].

The goal of this paper is to develop a methodology able to separate SF and muscle impedivity properties from sEIM data. To do so, we first evaluate SS techniques ICA and PCA. Then, a new model component analysis (MCA) technique is presented. Here, MCA introduces the prior knowledge in the framework by using a model function connecting the source signals with the observation –in other words, the impedivity of SF and muscle tissues are connected to the frequency measured. Then, the MCA estimation problem is formulated as minimization of the distance between the model function and a new family of input functions. Simulations using experimental data and measurements in diseased individuals confirm the usefulness of the novel MCA presented.

II. Signal Separation Techniques: Model Component Analysis

In this paper we will deal with the separation problem using the following linear model

$$\mathbf{x}(t) = \mathbf{A}\mathbf{s}(t), \tag{1}$$

where $\mathbf{x}(t) = [x_1(t), x_2(t), \ldots, x_O(t)]^\top$ represents a vector of measured signals ($(\bullet)^\top$ denotes the transpose operator), $\mathbf{A}$ is the unknown $O \times N$ mixing matrix, $\mathbf{s}(t) = [s_1(t), s_2(t), \ldots, s_N(t)]^\top$ represents a vector of source signals; with N and O being the number of source and mixed signals, respectively. The problem set by SS may be summarized as follows. Given the observations of mixed signals $\mathbf{x}$, it is desired to estimate (separate) the corresponding source signals $\mathbf{s}$, where the mixing matrix $\mathbf{A}$ is unknown.

Below, we introduce ICA and PCA methods so that MCA can be compared to these two SS techniques. Before delving into their specific application to EIM, we first introduce the methods in the context of the "cocktail party problem", a well-known application of SS techniques [18]. Here, the voice (source signals) from different people are separated from the recorded signals (e.g., using microphones) consisting of people talking simultaneously in the same room (mixed signals). We consider two sets of mixed signals $\mathbf{x}_{12} = [x_1, x_2]^\top$ and $\mathbf{x}_{34} = [x_3, x_4]^\top$ defined as, $x_1(t) := 0.7s_1(t) + 0.3s_2(t)$, $x_2(t) := 0.5s_1(t) + 0.5s_2(t)$, $x_3(t) := 0.7s_3(t) + 0.3s_4(t)$ and $x_4(t) := 0.5s_3(t) + 0.5s_4(t)$, where the source signals are

$$\begin{cases} s_1(t) := 3\sin(2t) + 4 \\ s_2(t) := 2\sin(3t) + 1, \end{cases}$$

for $t \in [0, 2\pi]$ and

$$\begin{cases} s_3(t) := 3\exp(t/2) + 1 \\ s_4(t) := 2\exp(t/3) + 4, \end{cases}$$

for $t \in [-6, 4]$. The source signals above were chosen to be representative of the cases where the source signals have small $s_{\{1,2\}}(t)$ and large $s_{\{3,4\}}(t)$ correlation between them. Below, we detail the settings of ICA (Section II-A), PCA (Section II-B), and the new MCA technique (Section II-C) and compare their performance (Section II-D).

A. Independent Component Analysis (ICA)

The working principle of ICA consists of decomposing the mixed signals into statistically independent signals [19]. Then, the ICA criterion to estimate the row vector $\mathbf{w}^\top$ of the unmixing matrix $\mathbf{W}$ is by maximizing nongaussianity of the signal $\mathbf{v}^\top\mathbf{x}$ from the mixed signal $\mathbf{x}$ as follows

$$\mathbf{v}_n := \arg\max_{\|\mathbf{v}\|^2=1} J(\mathbf{v}^\top\mathbf{x}), \tag{2}$$

where $n = 1, 2, \ldots, N$, $\|\bullet\|$ is the L2-norm, and $J(y)$ is a measure of non-gaussianity of the variable y, which is independent from the observation t. Examples of nongaussianity functions of J are normalized kurtosis and negentropy functions [20]. Note there can be N possible distinct local maxima in (2), i.e., $\{\mathbf{v}_n\}_{n=1}^N$. Thus, ICA requires to decorrelate the estimated source signals $\{\mathbf{w}_n^\top\mathbf{x}\}_{n=1}^N$, for example, applying Gram-Schmidt process

$$\mathbf{u}_n := \mathbf{v}_n - \sum_{j=1}^{n-1} \mathbf{v}_n^\top\mathbf{w}_j\mathbf{w}_j, \tag{3}$$

where $\mathbf{w}_j := \mathbf{u}_j/\|\mathbf{u}_j\|$.

The source signals estimated with ICA are based on the algorithm described in [21] using the approximated negentropy $J(y) := (\mathbb{E}\langle H(y) - \mathbb{E}H(v)\rangle)^2$ [22], where v is a Gaussian variable of zero mean and unit variance, $H(y) = -\exp(-y^2/2)$ is a nonquadratic function and $\mathbb{E}\bullet$ is the expected value operator.

B. Principal Component Analysis (PCA)

The basis of PCA is to convert the correlated mixed signals into a set of values of linearly uncorrelated variables, the so-called principal components. Then, the PCA criterion to estimate the n-th unmixing row vector $\mathbf{w}_n$ giving n-th principal component consists of maximizing the variances of the mixed

signal as follows

$$\mathbf{w}_n := \arg\max_{\|\mathbf{w}\|^2=1} J(\mathbf{w}^\top \mathbf{x}_n), \tag{4}$$

where $J(y) = \|y\|^2$, $\mathbf{x}_n := (\mathbf{I} - \sum_{j=1}^{n-1} \mathbf{w}_j \mathbf{w}_j^\top)\mathbf{x}$ is a generated signal from mixed signal $\mathbf{x}$ and unmixing row vector $\{\mathbf{w}_j\}_{j=1}^{n-1}$, with $n = 1, 2, \ldots, N$, and $\mathbf{I}$ is the identity matrix with size $N \times N$. When $n = 1$, the first principal component has the largest possible variance that can be obtained. For $n = 2, 3, \ldots, N$, the consecutive principal components have the largest variance possible under the constraint that it is orthogonal to the preceding principal components.

We used singular value decomposition to obtain the unmixing matrix $\mathbf{W} = \mathbf{U}\mathbf{\Lambda}$ which satisfies (4), with $\mathbf{x} = \mathbf{U}\mathbf{\Lambda}\mathbf{V}^\top$, and where $\mathbf{\Lambda}$ is a rectangular diagonal matrix of singular values with size $2 \times T$, $\mathbf{U}$ is matrix with orthonormal left singular vectors with size 2×2, and $\mathbf{V}$ is a matrix with orthonormal right column vectors with size $T \times T$, and T is the number of observations.

C. Model Component Analysis (MCA)

The MCA considers the dependence between the variable y and the observation t through the model function $\eta(t)$. Here, J is a model metric function that measures the distance between the input function $y = f(t)$ and the model function $\eta(t)$. Then, the MCA criterion consists of minimizing J from the mixed signal vector as follows

$$\mathbf{v}_n := \arg\min_{\|\mathbf{v}\|^2=1} J(\mathbf{v}_n^\top \mathbf{x}, t), \tag{5}$$

where the definition of J depends on the model function $\eta(t)$. From (5) using (3) we can obtain $\mathbf{w}_n$ for $n = 1, 2, \ldots, N$.

One possible approach is to define $\eta(t)$ in (5) as

$$J(y, t) := (\mathbb{E}\langle \mathscr{H}(y, t)\rangle)^2. \tag{6}$$

Then, $\mathscr{H}(y, t)$ is a suitable functional establishing an algebraic relationship between the model function $\eta(t)$ and its derivative and/or integral forms so that $\mathscr{H}(y, t)$ will be zero for $y = \eta(t)$. For example, if we consider $\eta(t) = \sin(t)$, then one suitable definition is $\mathscr{H}(y, t) = y^2 + (dy/dt)^2 - 1$. On the other hand, if $\eta(t) = \exp(t)$, then one appropriate candidate is $\mathscr{H}(y, t) = y - (dy/dt)$. Lastly, if we consider $\eta(t) = p_n(t)$ as n-th order polynomial, a reasonable model metric function is $\mathscr{H}(y, t) = y^{n-1} - (dy/dt)^n$.

We consider the model metric function in (6) to separate the mixed signals $x_{\{1,\ldots,4\}}(t)$. In particular, to separate the mixed signals $x_{\{1,2\}}(t)$, we use the model function $\eta(t) = a\sin(bt) + c$ for $a, b, c \in \mathbb{R}$. By the Pythagorean trigonometric identity, one can find $(\eta(t) - c)^2 - \eta'(t)\Psi(t) - a^2 = 0$ where $\Psi(t) := \int(\eta(t) - c)\, dt$ with $\max\{\Psi\} + \min\{\Psi\} = 0$. In this case, the functional evaluated is

$$\mathscr{H}(y, t) = (y(t) - \tilde{c})^2 - y'(t)Y(t) - \tilde{a}^2,$$

with $Y(t) := \int(y(t) - \tilde{c})\, dt - (\max\{Y\} + \min\{Y\})/2$, $\tilde{a} := (\max\{y\} - \min\{y\})/2$ and $\tilde{c} := (\max\{y\} + \min\{y\})/2$.

Next, to separate the mixed signals $x_{\{3,4\}}(t)$, we use the model function $\eta(t) = a\exp(bt) + c$ for $a, b, c \in \mathbb{R}$. It can be easily shown that $\eta'(t)\Psi(t) = (\eta(t))^2$ where $\Psi(t) := \int(\eta(t) - c)\, dt$ with $\Psi(t) \to 0$ as $t \to -\infty$. Then, the functional used is

$$\mathscr{H}(y, t) = y'(t)Y(t) - (y(t) - \tilde{c})^2,$$

with $\tilde{c} := \lim_{t\to-\infty} y(t)$ and $Y(t) := \int(y(t) - \tilde{c})\, dt$ with $Y(t) \to 0$ as $t \to -\infty$.

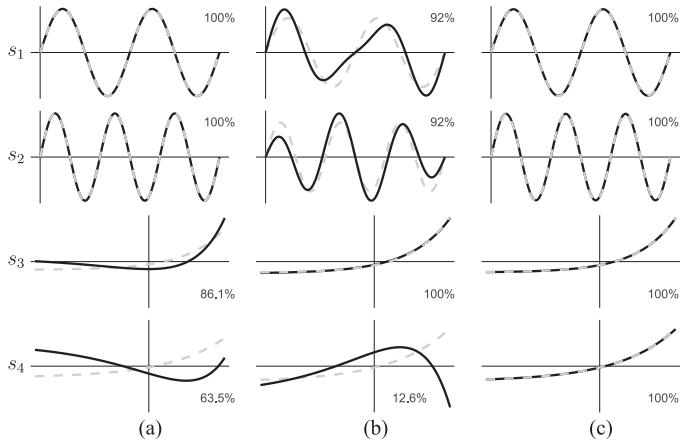

Fig. 1. In solid black lines, the estimated centered and whitened source signals. (a) Using independent component analysis (ICA). (b) Using principal component analysis (PCA). (c) Using model component analysis (MCA). The original centered and whitened source signals are shown in gray dotted lines for comparison purposes. The values on the abscissa representing time are omitted for clarity. The percentages shown indicate the similarity between original and estimated source signals for each case, being 0% if totally different and 100% if perfectly alike.

D. Benchmark Results

To facilitate the comparison between SS methods, both the original and estimated source signals were centered (zero-mean) and normalized to unit variance. We then calculated the absolute value of the correlation (0% to 100% scale) between the true source signals and the estimated source signals to compare the performance between methods. As expected, ICA (figure 1(a)) can separate the source signals when they are are poorly correlated as $s_{\{1,2\}}(t)$ and fails when the source signals are correlated as $s_{\{3,4\}}(t)$. On the other hand, PCA (figure 1(b)) can separate one dependent source signal $s_3(t)$ but not $s_4(t)$ or $s_{\{1,2\}}(t)$. Finally, MCA (figure 1(c)) is able to separate all the source signals.

III. Signal Separation Techniques Applied to Surface Electrical Impedance Myography

Next, we derive the linear system in (1) starting from the impedance governing equation (7) including electrodes' contact impedance. Injecting a sinusoidal electrical current with amplitude $I \in \mathbb{R}$ (A) between the current electrodes I^+ and I^- induces an electrical potential $u^I \in \mathbb{C}$ (V), which can be

described as follows

$$\begin{cases} \nabla \cdot (\gamma \nabla u^I) = 0 \quad \text{in } \mathscr{D}, \\ u^I + z_\ell \gamma \dfrac{\partial u^I}{\partial \mathbf{n}}\bigg|_\ell = P_\ell \quad \text{for } \ell = I^+, I^-, V^+, V^-, \\ \int_{I^+} \gamma \dfrac{\partial u^I}{\partial \mathbf{n}}\, ds = I = -\int_{I^-} \gamma \dfrac{\partial u^I}{\partial \mathbf{n}}\, ds, \\ \int_\ell \gamma \dfrac{\partial u^I}{\partial \mathbf{n}}\, ds = 0 \quad \text{for } \ell = V^+, V^-, \\ \gamma \dfrac{\partial u^I}{\partial \mathbf{n}} = 0 \quad \text{on } \partial\mathscr{D} \setminus (I^+ \cup I^- \cup V^+ \cup V^-), \end{cases} \tag{7}$$

where V^+ and V^- are the voltage electrodes, $\gamma(\omega) = \sigma(\omega) + i\omega\epsilon_0\epsilon_r(\omega)$ is the admittivity with $\sigma \in \mathbb{R}$ (S m^{-1}) and $\epsilon_r \in \mathbb{R}$ (dimensionless) the conductivity and relative permittivity properties of the conductor domain $\mathscr{D} \in \mathbb{R}^3$ (m^3), respectively, ϵ_0 is the vacuum permittivity (F m^{-1}), $\omega \in \mathbb{R}$ is the (angular) frequency dependence (rad s^{-1}), $i := \sqrt{-1}$ is the imaginary unit (dimensionless), $\mathbf{n}$ is the outward unit normal vector to the boundary $\partial\mathscr{D}$, z_ℓ is the electrodes' contact impedance, and P_ℓ is the corresponding constant potential on the electrode ℓ for $\ell = I^\pm, V^\pm$ [23].

Then, if the electrodes are in contact with an homogenous domain (e.g., SF $\mathscr{D}_{\mathrm{sf}}$ or muscle $\mathscr{D}_{\mathrm{m}}$ tissue), the impedance measured $Z \in \mathbb{C}$ (Ω) between V^+ and V^- electrodes satisfies that [24]

$$Z = R + iX = \kappa S = \kappa \int_{\mathscr{D}} \mathbf{J}^I \cdot \mathbf{J}^V \, d\mathbf{r}, \tag{8}$$

where $R \in \mathbb{R}$ and $X \in \mathbb{R}$ are the resistance and reactance measured, $\kappa(\omega) := \rho(\omega) + i\tau(\omega) = 1/\gamma(\omega)$ is the impedivity (Ω m) of the domain, ρ and τ are the resistivity and reactivity, respectively, $S \in \mathbb{C}$ is the *impedance* sensitivity (m^{-1}) [11] which depends on $\{\mathscr{D}, \kappa, \omega\}$ and the electrodes' characteristics, and $\mathbf{J}^{\{I,V\}} \in \mathbb{C}$ (m^{-2}) are the local current density vectors found swapping the injection of electrical current between the current and voltage electrodes, respectively.

In this paper, we consider an heterogenous domain made of homegenous SF and muscle sub-domains, i.e., $\mathscr{D} := \mathscr{D}_{\mathrm{sf}} \cup \mathscr{D}_{\mathrm{m}}$. One important feature of these tissues is the directional dependence of their impedivity properties. Thus, a realistic approach is to assume SF as an isotropic tissue (i.e., the impedivity is the same in all directions), and muscle as an anisotropic tissue (the impedivity is different in longitudinal –L– and transverse –T– directions with respect to the fibers' orientation) [25]. Therefore, considering the x-direction as the longitudinal direction in the muscle, we can rewrite the impedance sensitivity in the muscle according to (8) as follows

$$\begin{aligned} S_{\mathrm{m}} &= \int_{\mathscr{D}_{\mathrm{m}}} \mathbf{J}^I \cdot \mathbf{J}^V \, d\mathbf{r} \\ &= \underbrace{\int_{\mathscr{D}_{\mathrm{m}}} J_1^I J_1^V \, d\mathbf{r}}_{=:S_{\mathrm{mL}}} + \underbrace{\int_{\mathscr{D}_{\mathrm{m}}} J_2^I J_2^V \, d\mathbf{r} + \int_{\mathscr{D}_{\mathrm{m}}} J_3^I J_3^V \, d\mathbf{r}}_{=:S_{\mathrm{mT}}}, \end{aligned} \tag{9}$$

where S_{mL} and S_{mT} are the sensitivity in the muscle in longitudinal and transverse directions, respectively.

We now assume sensitivity S in SF and muscle tissues is complex constant number. Then, by combining (8) and (9) with $P := \mathrm{Re}(S)$, $Q := \mathrm{Im}(S)$ one finds

$$\begin{cases} R(\omega_k) = \rho_{\mathrm{sf}}(\omega_k)P_{\mathrm{sf}} - \tau_{\mathrm{sf}}(\omega_k)Q_{\mathrm{sf}} \\ \qquad\quad +\rho_{\mathrm{mT}}(\omega_k)P_{\mathrm{mT}} - \tau_{\mathrm{mT}}(\omega_k)Q_{\mathrm{mT}} \\ \qquad\quad +\rho_{\mathrm{mL}}(\omega_k)P_{\mathrm{mL}} - \tau_{\mathrm{mL}}(\omega_k)Q_{\mathrm{mL}} \\ X(\omega_k) = \rho_{\mathrm{sf}}(\omega_k)Q_{\mathrm{sf}} + \tau_{\mathrm{sf}}(\omega_k)P_{\mathrm{sf}} \\ \qquad\quad +\rho_{\mathrm{mT}}(\omega_k)Q_{\mathrm{mT}} + \tau_{\mathrm{mT}}(\omega_k)P_{\mathrm{mT}} \\ \qquad\quad +\rho_{\mathrm{mL}}(\omega_k)Q_{\mathrm{mL}} + \tau_{\mathrm{mL}}(\omega_k)P_{\mathrm{mL}}, \end{cases} \tag{10}$$

where ω_k is the (angular) frequency (rad s^{-1}) measured, $k = 1, \ldots, F$ is the frequency index, and F is the number of frequencies measured. The subscripts sf and m denote the resistivity, reactivity and sensitivity in the SF and muscle tissues, respectively. As mentioned above, these tissues' properties are different over the frequency. Equation (10) can be written in a matrix form when the impedance is measured using different electrode configurations, namely

$$\begin{bmatrix} \vdots & \vdots & \vdots & \vdots & \vdots & \vdots \\ P_{\mathrm{sf}}^{[m]} & P_{\mathrm{mT}}^{[m]} & P_{\mathrm{mL}}^{[m]} & -Q_{\mathrm{sf}}^{[m]} & -Q_{\mathrm{mT}}^{[m]} & -Q_{\mathrm{mL}}^{[m]} \\ Q_{\mathrm{sf}}^{[m]} & Q_{\mathrm{mT}}^{[m]} & Q_{\mathrm{mL}}^{[m]} & P_{\mathrm{sf}}^{[m]} & P_{\mathrm{mT}}^{[m]} & P_{\mathrm{mL}}^{[m]} \\ \vdots & \vdots & \vdots & \vdots & \vdots & \vdots \end{bmatrix} \begin{bmatrix} \rho_{\mathrm{sf}}(\omega_k) \\ \rho_{\mathrm{mT}}(\omega_k) \\ \rho_{\mathrm{mL}}(\omega_k) \\ \tau_{\mathrm{sf}}(\omega_k) \\ \tau_{\mathrm{mT}}(\omega_k) \\ \tau_{\mathrm{mL}}(\omega_k) \end{bmatrix} = \begin{bmatrix} \vdots \\ R^{[m]}(\omega_k) \\ X^{[m]}(\omega_k) \\ \vdots \end{bmatrix}, \tag{11}$$

where the superscript $[\bullet]$ differentiates from exponentiation and denotes the m-th electrode configuration used to measure impedance, for $m = 1, \ldots, M$, and where M is the number of different tetrapolar electrode configurations measured (see the different electrodes configurations in figure 2).

The size of (11) can be reduced by introducing the anisotropy ratio between the longitudinal and transverse resistivity and reactivity in the muscle, i.e., $\lambda^2\rho_{\mathrm{mT}} = \rho_{\mathrm{mL}}$ and $\mu^2\tau_{\mathrm{mT}} = \tau_{\mathrm{mL}}$

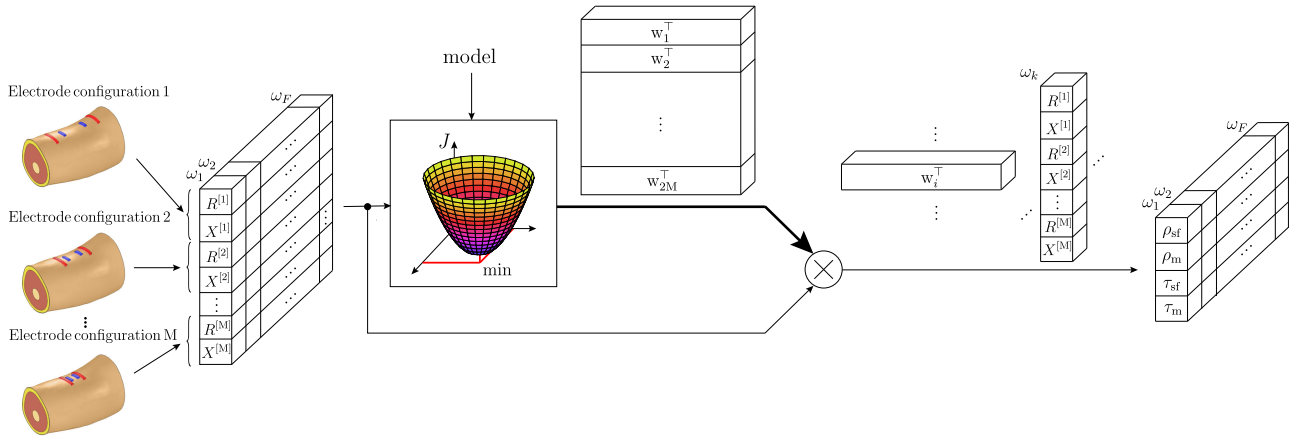

Fig. 2. Flowchart illustrating the working principle of model component analysis applied to surface electrical impedance myography (sEIM). The algorithm's input data $\mathbf{z}$ at frequency ω_k with $k = 1, \ldots, F$ frequencies are measured using at least two ($M \geq 2$) electrodes' configurations, for example, with the same orientation and different separation between current I^+, I^- and voltage V^+, V^- electrodes (shown in red and blue color, respectively). These data together with the known physical model are used to minimize the user-defined model metric function J. The result of this minimization procedure is the unmixing matrix $\mathbf{W}$ (illustrated by a thick black line) used to separate the resistivity and reactivity parts of subcutaneous fat $\rho_{\mathrm{sf}}, \tau_{\mathrm{sf}}$ and muscle $\rho_{\mathrm{m}}, \tau_{\mathrm{m}}$ tissues.

[26], namely

$$\underbrace{\begin{bmatrix} \vdots & \vdots & \vdots & \vdots \\ P_{\mathrm{sf}}^{[m]} & (P_{\mathrm{mT}}^{[m]} + \lambda^2 P_{\mathrm{mL}}^{[m]}) & -Q_{\mathrm{sf}}^{[m]} & -(Q_{\mathrm{mT}}^{[m]} + \mu^2 Q_{\mathrm{mL}}^{[m]}) \\ Q_{\mathrm{sf}}^{[m]} & (Q_{\mathrm{mT}}^{[m]} + \lambda^2 Q_{\mathrm{mL}}^{[m]}) & P_{\mathrm{sf}}^{[m]} & (P_{\mathrm{mT}}^{[m]} + \mu^2 P_{\mathrm{mL}}^{[m]}) \\ \vdots & \vdots & \vdots & \vdots \end{bmatrix}}_{=:\mathbf{S}}$$

$$\underbrace{\begin{bmatrix} \rho_{\mathrm{sf}}(\omega_k) \\ \rho_{\mathrm{mT}}(\omega_k) \\ \tau_{\mathrm{sf}}(\omega_k) \\ \tau_{\mathrm{mT}}(\omega_k) \end{bmatrix}}_{=:\boldsymbol{\kappa}(\omega_k)} = \underbrace{\begin{bmatrix} \vdots \\ R^{[m]}(\omega_k) \\ X^{[m]}(\omega_k) \\ \vdots \end{bmatrix}}_{=:\mathbf{z}(\omega_k)} \tag{12}$$

or, simply

$$\mathbf{S}\boldsymbol{\kappa} = \mathbf{z}, \tag{13}$$

where $\mathbf{S}$ is the mixing sensitivity matrix with size $2M \times N$, $\boldsymbol{\kappa}$ is the source signal vector composed of the impedivity of SF and muscle tissues with size $N \times 1$, and $\mathbf{z}$ is the mixed signal vector (input data) containing valid and meaningful impedance (i.e., resistance and reactance) values measured with size $2M \times 1$. Note that in order to build $\mathbf{z}$, each pair of resistance and reactance data can be generated from an impedance measurement in which the electrodes' array orientation is kept the same and the distance between current I^+, I^- and voltage V^+, V^- electrodes is changed, the electrodes' size is changed, or both.

Then, the solution to (13) can be stated as follows

$$\boldsymbol{\kappa} = \mathbf{W}\mathbf{z}, \tag{14}$$

where $\mathbf{W}$ is the unknown unmixing matrix with size $N \times 2M$ and $\boldsymbol{\kappa}$ is the estimated source signal vector. For convenience, here we consider the case where $\mathbf{W} = \mathbf{S}^{-1}$ and so $2M = N$ (i.e., square matrix).

Next, we attempt to obtain $\boldsymbol{\kappa}$ in (14) using ICA, PCA, and MCA. At this point, we note a common practice in bioimpedance studies is to consider only the resistive part of bioimpedance ($\rho \neq 0$ and $\tau = 0$ as in [27]). Here, however, we have studied also the reactive case ($\rho = 0$ and $\tau \neq 0$) and the more general case where the bioimpedance consists of both components ($\rho \neq 0$ and $\tau \neq 0$). For ICA and PCA, we used the mixing matrices in Section V and the same algorithms described in Section II-A and II-B, respectively. Below, we introduce the physical model and analyze in detail MCA for the three cases mentioned above.

A. Model Component Analysis (MCA)

1) Physical Model: The equivalent electrical circuit proposed by Fricke and Morse in [28] is a model widely used to analyze the bioimpedance of living biological tissues [29]–[32]. The model is described by a series resistor-capacitor network in parallel with a resistor, namely

$$\kappa(\omega) = \frac{r_{\mathrm{e}} + i\omega r_{\mathrm{e}} r_{\mathrm{i}} c_{\mathrm{m}}}{1 + i\omega c_{\mathrm{m}}(r_{\mathrm{e}} + r_{\mathrm{i}})}, \tag{15}$$

where $\kappa(\omega)$ is the tissue's impedivity, $r_{\{\mathrm{e,i}\}}$ (Ω m) represent the effective resistivity of the extra- and intra-cellular media, respectively, and c_{m} (F m^{-2}) represents the cells' surface membrane capacitance. Equation (15) can be splitted into real and imaginary parts,

$$\kappa(\omega) = \frac{r_2 + r_1 r_3 \omega^2}{1 + r_3^2 \omega^2} + i\frac{(r_1 - r_2 r_3)\omega}{1 + r_3^2 \omega^2}, \tag{16}$$

where $r_1 := r_{\mathrm{e}} r_{\mathrm{i}} c_{\mathrm{m}}$, $r_2 := r_{\mathrm{e}}$, $r_3 := (r_{\mathrm{e}} + r_{\mathrm{i}}) c_{\mathrm{m}}$. To facilitate the separation of the source signals over the frequency ω, it is convenient to model the resistivity and reactivity using the

logarithm of the angular frequency $\varpi := \log_{10}\omega$ so that

$$\overline{\rho}(\varpi) = a_\rho + \frac{b_\rho}{10^{2\varpi} + c_\rho}, \tag{17}$$

with $a_\rho := r_1/r_3$, $b_\rho := r_2/r_3^2 - r_1/r_3^3$ and $c_\rho := 1/r_3^2$; and

$$\overline{\tau}(\varpi) = \frac{b_\tau 10^{\varpi}}{10^{2\varpi} + c_\tau}, \tag{18}$$

with $b_\tau := (r_1 - r_2 r_3)/r_3^2$ and $c_\tau := 1/r_3^2$.

2) Resistive Part: The mixed signal vector $\mathbf{z}$ was computed using $\kappa = [\rho_{\mathrm{sf}}\ \rho_{\mathrm{mT}}]^\top$ and the mixing matrix $\mathbf{S}_\rho$ in Section IV-A. To design the model metric function $J_{\overline{\rho}}$, we need to approximate the unknown a and b constants using the input function $y = f(t)$, for example

$$\widetilde{a}_{\overline{\rho}} := \lim_{t\to\infty} f(t),\ \widetilde{b}_{\overline{\rho}} := \lim_{t\to\infty}(f(t) - \widetilde{a})T^{2t} \text{ or } \lim_{t\to\infty} -\frac{1}{2T_e} f'(t)T^{2t}, \tag{19}$$

with $T := 10$. The requirement $t \to \infty$ to estimate $\widetilde{a}$ and $\widetilde{b}$ in (19) implies in practice to measure the bioimpedance at high frequency, e.g., 1 MHz. Then, we can define the following functionals

$$\begin{aligned}
\mathscr{H}_{\overline{\rho},d1}(y,t) &:= (y - \widetilde{a}_{\overline{\rho}}) - \left(\widetilde{k}_{\overline{\rho}} y_{d1} T^{-2t}\right)^{1/2} \\
\mathscr{H}_{\overline{\rho},d2}(y,t) &:= (y - \widetilde{a}_{\overline{\rho}}) - \left((\widetilde{k}_{\overline{\rho}}/2) y_{d2} T^{-2t}\right)^{1/3} \\
\mathscr{H}_{\overline{\rho},i1}(y,t) &:= (y - \widetilde{a}_{\overline{\rho}}) - y_{i1}/\widetilde{k}_{\overline{\rho}} \\
\mathscr{H}_{\overline{\rho},i2}(y,t) &:= (y - \widetilde{a}_{\overline{\rho}}) - y_{i2}/\widetilde{k}_{\overline{\rho}},
\end{aligned} \tag{20}$$

which all give zero-function when the input function $y = f(t)$ matches the resistivity function $\overline{\rho}(\varpi)$ in (17), and where $y_{d1} := \frac{d}{dt}y$, $y_{d2} := \widetilde{k}_{\overline{\rho}}\frac{d}{dt}(y_{d1}T^{-2t})$, $y_{i1} := \int((y - \widetilde{a})T^t)^2 dt$, $y_{i2} := (1/\widetilde{k})^2 \int (y_{i1}T^t)^2 dt$, and $\widetilde{k}_{\overline{\rho}} := -\frac{\widetilde{b}_{\overline{\rho}}}{2\ln 10}$. Finally, the model metric function $J_{\overline{\rho}}$ can be defined using just one or a combination of the functionals in (20). Here, we use the mean root mean square of the functionals' expected values, namely

$$J_{\overline{\rho}}(y,t) := \frac{1}{2}\sqrt{\sum_{n=1}^{2} \mathbb{E}\langle \mathscr{H}_{\overline{\rho},d\{n\}}(y,t)\rangle^2 + \sum_{n=1}^{2} \mathbb{E}\langle \mathscr{H}_{\overline{\rho},i\{n\}}(y,t)\rangle^2}. \tag{21}$$

3) Reactive Part: The mixed signal vector $\mathbf{z}$ was computed using $\kappa = [\tau_{\mathrm{sf}}\ \tau_{\mathrm{mT}}]^\top$ and the mixing matrix $\mathbf{S}_\tau$ in Section IV-A. To design the model metric function $J_{\overline{\tau}}$, we need to approximate b with the input function $y = f(t)$, for example

$$\widetilde{b}_{\overline{\tau}} := \lim_{t\to\infty} f(t)T^t. \tag{22}$$

In the same way as the purely resistive case (see Section III-A2), it is necessary to measure the bioimpedance at high frequencies in order to obtain an accurate estimate in (22). Then, we define the following functionals

$$\begin{aligned}
\mathscr{H}_{\overline{\tau},d1}(y,t) &:= yT^{-t} - \left(\widetilde{k}_{\overline{\tau}} y_{d1} T^{-2t}\right)^{1/2} \\
\mathscr{H}_{\overline{\tau},d2}(y,t) &:= yT^{-t} - \left((\widetilde{k}_{\overline{\tau}}/2) y_{d2} T^{-2t}\right)^{1/3} \\
\mathscr{H}_{\overline{\tau},i1}(y,t) &:= yT^{-t} - y_{i1}/\widetilde{k}_{\overline{\tau}} \\
\mathscr{H}_{\overline{\tau},i2}(y,t) &:= yT^{-t} - y_{i2}/\widetilde{k}_{\overline{\tau}},
\end{aligned}$$

which all give zero-function when the input function $y = f(t)$ matches the reactivity function $\overline{\tau}(\varpi)$ in (18), and where $y_{d1} := \frac{d}{dt}(yT^{-t})$, $y_{d2} := \widetilde{k}_{\overline{\tau}}\frac{d}{dt}(y_{d1}T^{-2t})$, $y_{i1} := \int y^2 dt$, $y_{i2} := (1/\widetilde{k}_{\overline{\tau}})^2 \int (y_{i1}T^t)^2 dt$, and $\widetilde{k}_{\overline{\tau}} := -\frac{\widetilde{b}_{\overline{\tau}}}{2\ln 10}$. Finally, an example of model metric function $J_{\overline{\tau}}$ can be calculated using the square root mean of the functionals' expected values, namely

$$J_{\overline{\tau}}(y,t) := \frac{1}{2}\sqrt{\sum_{n=1}^{2} \mathbb{E}\langle \mathscr{H}_{\overline{\tau},d\{n\}}(y,t)\rangle^2 + \sum_{n=1}^{2} \mathbb{E}\langle \mathscr{H}_{\overline{\tau},i\{n\}}(y,t)\rangle^2}. \tag{23}$$

4) Resistive and Reactive Parts: The mixed signal vector $\mathbf{z}$ was computed using $\kappa = [\rho_{\mathrm{sf}}\ \rho_{\mathrm{mT}}\ \tau_{\mathrm{sf}}\ \tau_{\mathrm{mT}}]^\top$ in and the mixing matrix $\mathbf{S}$ in Section IV-A. We then use (21) and (23) to estimate the source signals.

IV. Materials and Methods

A. Simulations

We confirmed the usefulness of MCA through simulations (MATLAB, The Mathworks, Natick, MA, USA) using experimental impedivity values from SF and muscle tissues $\boldsymbol{\kappa}$ measured from 1 kHz to 1 MHz (151 frequencies/observations). The experimental impedivity values of tissues were obtained from an online reference database [33]. The mixing matrices $\mathbf{S}_\rho$ ($\rho \neq 0$ and $\tau = 0$), $\mathbf{S}_\tau$ ($\rho = 0$ and $\tau \neq 0$), and $\mathbf{S}$ ($\rho \neq 0$ and $\tau \neq 0$), were calculated using the finite element method (FEM) (Comsol Multiphysics, Inc., Burlington, MA, USA) at 1 kHz and assumed constant over the frequency. The FEM simulations included reference electrodes' contact impedance at 1 kHz obtained from AgCl pre-gelled wet electrolyte electrodes with surface resistance $10^{-3}\ \Omega\ \mathrm{m}^2$ and surface capacitance $0.16 \cdot 10^{-6}\ \mathrm{F\ m}^2$ [1]. The resulting sensitivity matrices are

$$\mathbf{S}_\rho = \mathbf{S}_\tau = \begin{bmatrix} 1.1775 & 5.2209 \\ 0.0509 & 5.9629 \end{bmatrix}$$

and

$$\mathbf{S} = \begin{bmatrix} 1.1775 & 5.2208 & 0.0002 & -0.0029 \\ -0.0002 & 0.0029 & 1.1775 & 5.2208 \\ 0.0509 & 5.9631 & 0.0001 & -0.0021 \\ -0.0001 & 0.0021 & 0.0509 & 5.9631 \end{bmatrix}.$$

We then calculated the mixed signals vector $\mathbf{z}$ in (13) using as source signals $\boldsymbol{\kappa}$ the resistivity and reactivity of SF and muscle tissues and the mixing matrices above. Finally, we added white

Gaussian noise with zero mean into (14) giving a signal-to-noise ratio (SNR) from 10 to 40 dB.

B. Experimental Protocol

This study was approved by the Institutional Review Board of Beth Israel Deaconess Medical Center. Ultrasound (US) imaging and impedance measurements were conducted in three convenience subjects participating in a separate clinical study (see clinicaltrials.gov NCT02104921). Informed consent was obtained from the subjects prior to the measurements. In all subjects (female, from 47 to 68 years old), the triceps brachii medius were measured since subjects had an increased SF thickness in the affected muscle.

C. Subject Information

Patients were diagnosed based on clinical history and examination supported by needle electromyography. Subject A was diagnosed with subacute right moderately severe cervical polyradiculopathy and had unilateral weakness on the right upper extremity. Then, Subject B had chronic, moderately severe ulnar neuropathy localized to the left elbow superimposed with a subacute, moderately severe left C7 radiculopathy. Subject C was diagnosed with myotonic dystrophy type II and had bilateral weakness.

D. Impedance Measurement and Analysis

For each patient, tetrapolar sEIM measurements ($n = 3$) were performed with SFB7 device (Impedimed, Inc., Brisbane, Australia) between 10 kHz and 1 MHz (203 frequencies) using two different electrode configurations. First, we used four 1.5-cm-wide $\times$ 2-cm-long gel-adhesive surface electrodes (70010-K/C/12, Ambu, Inc., Denmark), and then we used a custom-made tetrapolar 1-mm-wide $\times$ 1-mm-long electrode array on a printed circuit board (PCB). The electrode spacing in both electrodes' arrays was uniform, being 2 cm and 1 mm between the edge of adjacent electrodes, respectively. For measurements with PCB electrodes, we moistened the skin with saline solution using a gauze prior the measurements to ensure a good electrode contact (see figure 3).

The placement of impedance electrodes in the triceps muscle was made with the center of the muscle being located by palpation at a point approximately one-third the distance up from the antecubital fossa and olecreanon toward the acromion, respectively. Surface EIM measurements were made with the patient in prone position and the arms 15°abducted. The entire procedure took approximately 30 minutes to perform.

E. Quantitative Muscle Ultrasound Image Acquisition and Analysis

US images of the muscles were obtained using a Terason t3000 system (Teracorp, Inc., Burlington, MA, USA) to determine the thickness of subcutaneous fat at the impedance measurement site and assess for any evidence of muscle fibrosis/fat deposition that can occur as a consequence of disease. All images were acquired in transverse direction with respect to the orientation of the limb using a 10 MHz probe and analyzed using MATLAB. We quantified the standard median gray scale level values (GSL, dimensionless) from the region of interest (ROI) within muscle immediately below the layer of subcutaneous tissue and above bone. For the calculation of GSL, previous studies have shown that echointensity is best measured from the most superficial one-third of the ROI of the muscle when quantifying levels of pathology using US [34].

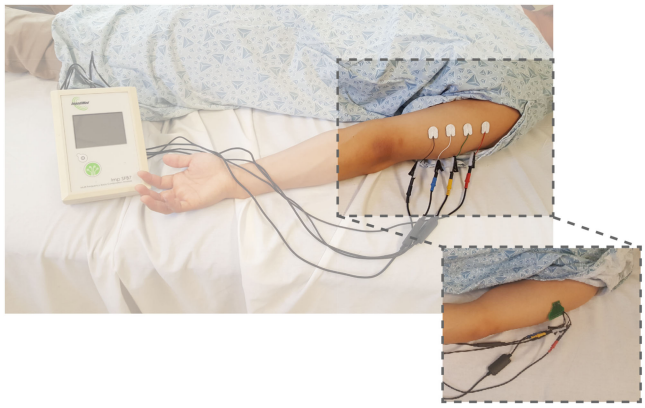

Fig. 3. Example of the experimental setup showing the placement of the electrodes (70010-K/C/12, Ambu, Inc., Denmark) and custom-made printed circuit board electrode array on a subject's right triceps brachii lying in prone position. Current and voltage electrodes were connected to the measuring device (SFB7, Impedimed, Inc., Brisbane, Australia) using crocodile clips.

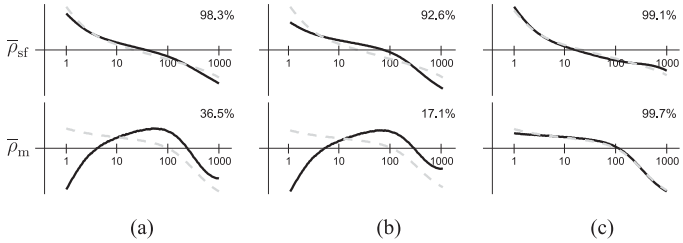

Fig. 4. Resistive part. In solid black lines, the noise-free estimated centered and whitened source signals. (a) using independent component analysis (ICA). (b) Using principal component analysis (PCA). (c) Using model component analysis (MCA). The original centered and whitened source signals are shown in gray dotted lines for comparison purposes. The values on the abscissa represent the frequency simulated (kHz) in logarithmic scale. The percentages shown indicate the similarity between original and estimated source signals for each case, being 0% if totally different and 100% if perfectly alike. Source signals: $\overline{\rho}_{\mathrm{sf}}$, resistivity of subcutaneous fat tissue; $\overline{\rho}_{\mathrm{m}}$, resistivity of muscle tissue.

V. Simulation Results

A. Resistive Part

The reader can see in figure 4 that ICA and PCA are only able to satisfactorily separate the resistivity of SF tissue with the similarity being 98.3% and 92.6%, respectively. MCA is capable of separating the resistivity of both SF and muscle tissues with the averaged similarity being 99.4%. Figure 5 then shows all three methods behave similarly at extracting only the resistivity of SF tissue from noisy sEIM data. However, MCA is the only

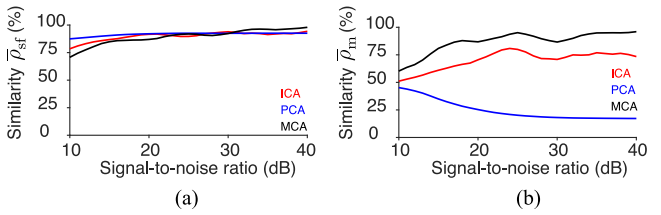

Fig. 5. Impact of measurement noise in the resistivity shown in Figure 4 using independent component analysis (ICA), principal component analysis (PCA), and model component analysis (MCA). Source signals. (a) $\overline{\rho}_{\mathrm{sf}}$, resistivity of subcutaneous fat tissue. $\overline{\rho}_{\mathrm{m}}$ (b) Resistivity of muscle tissue.

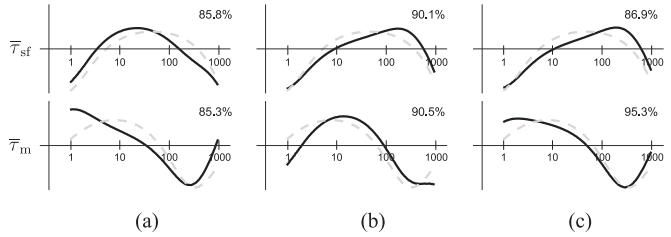

Fig. 6. Reactive part. In solid black lines, the estimated noise-free centered and whitened source signals. (a) Using independent component analysis (ICA). (b) Using principal component analysis (PCA). (c) Using model component analysis (MCA). The original centered and whitened source signals are shown in gray dotted lines for comparison purposes.The values on the abscissa represent the frequency simulated (kHz) in logarithmic scale. The percentages shown indicate the similarity between original and estimated noise-free source signals for each case, being 0% if totally different and 100% if perfectly alike. Source signals: $\overline{\tau}_{\mathrm{sf}}$, reactivity of subcutaneous fat tissue; $\overline{\tau}_{\mathrm{m}}$, reactivity of muscle tissue.

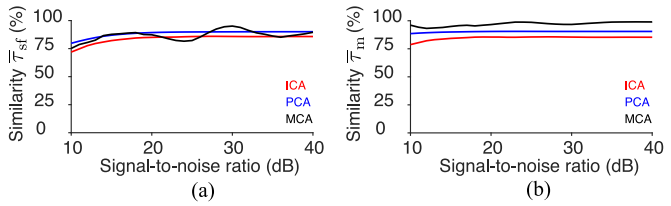

Fig. 7. Impact of measurement noise in the reactivity shown in figure 6 using independent component analysis (ICA), principal component analysis (PCA), and model component analysis (MCA). Source signals. (a) $\overline{\tau}_{\mathrm{sf}}$, reactivity of subcutaneous fat tissue. (b) $\overline{\tau}_{\mathrm{m}}$, reactivity of muscle tissue.

method capable of correctly separating also the resistivity of muscle tissue when the SNR equals or is greater than 20 dB.

B. Reactive Part

If we consider the reactivity of SF and muscle tissues, figure 6 shows that all three methods provide moderately correct results, being MCA the most accurate with averaged similarity being 91.1%, followed by PCA with 90.3% and finally ICA with 85.6%. As shown in Figure 7, all methods provide alike similarity when extracting SF tissue individually considering noise in the sEIM data. As for the separating muscle reactivity, MCA is the most accurate method followed by ICA and PCA.

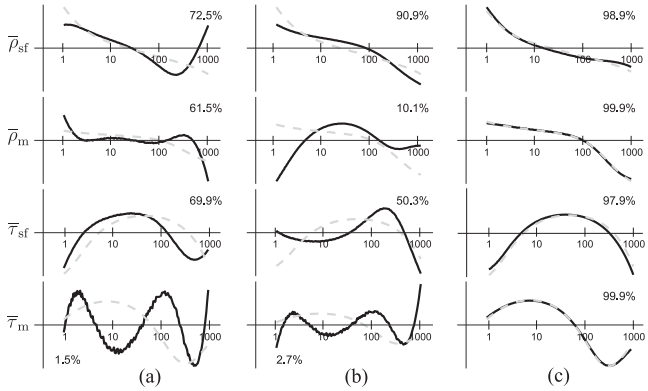

Fig. 8. Resistive and reactive parts. In solid black lines, the estimated noise-free centered and whitened source signals. (a) Using independent component analysis (ICA). (b) Using principal component analysis (PCA). (c) Using model component analysis (MCA). The original centered and whitened source signals are shown in gray dotted lines for comparison purposes. The values on the abscissa represent the frequency simulated (kHz) in logarithmic scale. The percentages shown indicate the similarity between original and estimated noise-free source signals for each case, being 0% if totally different and 100% if perfectly alike. Source signals: $\overline{\rho}_{\mathrm{sf}}$, resistivity of SF tissue; $\overline{\rho}_{\mathrm{m}}$, resistivity of muscle tissue; $\overline{\tau}_{\mathrm{sf}}$, reactivity of subcutaneous fat tissue; $\overline{\tau}_{\mathrm{m}}$, reactivity of muscle tissue.

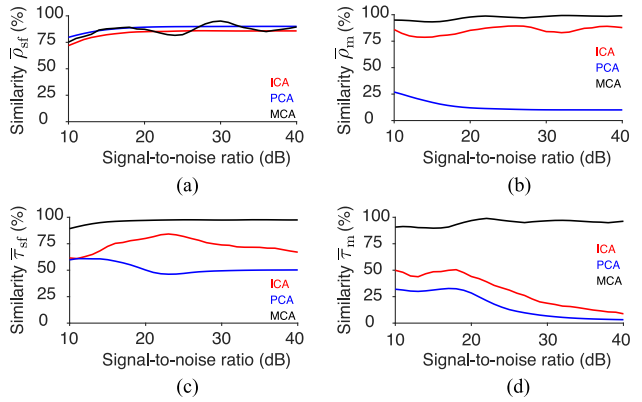

Fig. 9. Impact of measurement noise in the resistivity and reactivity shown in Figure 8 using independent component analysis (ICA), principal component analysis (PCA), and model component analysis (MCA). Source signals. (a) $\overline{\rho}_{\mathrm{sf}}$, resistivity of subcutaneous fat tissue. (b) $\overline{\rho}_{\mathrm{m}}$, resistivity of muscle tissue. (c) $\overline{\tau}_{\mathrm{sf}}$, reactivity of subcutaneous fat tissue. (d) $\overline{\tau}_{\mathrm{m}}$, reactivity of muscle tissue.

C. Resistive and Reactive Parts

Figure 8 shows the performance of ICA and PCA worsens when treating both the resistivity and reactivity parts combined with an averaged similarity being 51.4% and 38.5%, respectively. MCA results are the most accurate with the averaged similarity being 99.2%. Of the three methods, figure 9 shows MCA is the only approach capable of separating the impedivity of both SF and muscle tissues.

VI. Experimental Results

The three patients had a similar fat thickness. The GSL value for the triceps muscle for Subject A, B and C was 25 (left triceps, nondominant), 27 (right triceps, dominant) and 24 (right triceps,

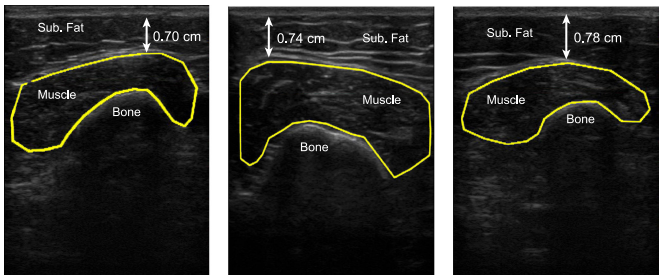

Fig. 10. Illustrative ultrasound images used to quantify subcutaneous fat thickness and gray scale levels (GSLs). We measured GSL from the most superficial one-third of the triceps' region of interest (delimited by the yellow lines). The arrows indicate the thickness of subcutaneous fat tissue at the impedance measurement site.

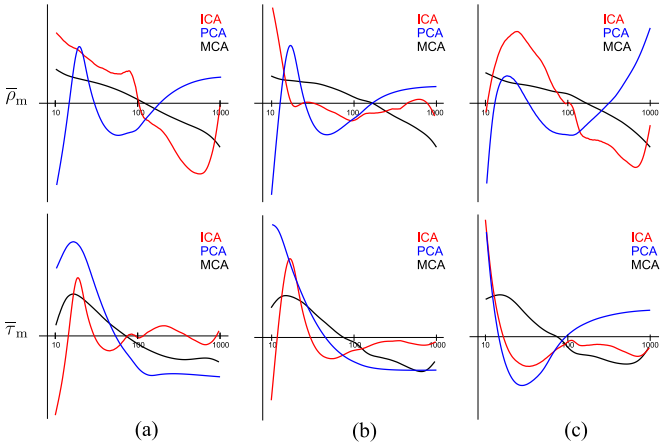

Fig. 11. Estimated centered and whitened source signals using independent component analysis (ICA, red), principal component analysis (PCA, blue), and model component analysis (MCA, black). The values on the abscissa represent the frequency measured (kHz) in logarithmic scale. Subcutaneous fat tissue' properties are not shown because it is not relevant to the diagnosis. Source signals: $\overline{\rho}_{\mathrm{m}}$, resistivity of muscle tissue; $\overline{\tau}_{\mathrm{m}}$, reactivity of muscle tissue.

dominant), respectively (see figure 10). These GSL values are within the range of normal values, suggesting that there has been no significant deposition of fat or connective tissue within the muscle. Deposition of such materials, usually in longstanding, more severe disease causes an elevation in GSL (i.e., the muscle become more echogenic and lighter in color). Figure 11 shows estimated muscle resistivity and reactivity from sEIM data using ICA, PCA and MCA. Despite pathological differences between subjects, GSL values were virtually the same thus indicating no significant changes in muscle composition between patients. Therefore, we did not expect to detect drastic changes between separated muscle resistivity and reactivity properties, which is consistent with the results shown in figure 11 using MCA. The interpretation of the results obtained with ICA and PCA should be made carefully, as discussed in the next section.

VII. Discussion

In this study, we have developed MCA to separate SF and muscle tissues' impedivity properties from sEIM measurements. Compared to existing separation methods such as ICA and PCA, our simulations and patients' measurements show that MCA is the only reliable method. Although we did not know the actual impedivity properties of diseased muscle (for example as measured ex vivo by biopsy), according to the Maxwell-Wagner polarization mechanism of dielectric relaxation observed in biological tissues [35], the dynamics of muscle resistivity must decrease monotonically with the frequency measured. However, the resistivity of muscle estimated using ICA and PCA increased within the measured frequency range. The similarity in muscle impedivity properties between patients using MCA is consistent with the GSL values obtained using US, the latter not revealing major alterations in muscle's composition.

Unlike ICA and PCA separation approaches that have been developed with weak statistical assumptions, MCA imposes a relationship between the frequency measured and the impedivity of the tissues by means of a physical model. Specifically, the key concept of MCA is the definition of the model metric function and the corresponding functional. According to the model function used, multiple possible definitions for the functional may exist. For example, here we defined the functional relating first- and second-order derivatives and integrals with approximated function parameters. Another possible approach would have been to increase the order of the derivatives. Although both approaches are theoretically analogous, in practice, the same analysis as the one presented relating the model metric function and functional through high-order derivatives led to algorithm instability (data not shown). Care should be taken in choosing the strategy to establish a relationship between them that leads to a stable algorithm implementation.

Ultimately, the goal in sEIM is to relate observed alterations in data with the muscle's cellular structure and composition. For example, myopathies may be characterized by inflammatory cells, edema, along with fat and connective tissue deposition. On the other hand, neurogenic diseases are associated predominantly with severe myofiber atrophy and fiber type grouping. These various characteristics will impact sEIM values in different ways. The challenge is to be able to detect these alterations from sEIM measurements that are obscured by SF tissue.

Indeed, SF tissue can make healthy muscle appear artificially abnormal or vice versa as shown in [11], obscuring the diagnosis or therapy response. A clinical case can provide context for this. For example, a young boy with DMD is placed on corticosteroids. Corticosteroids are known to improve muscle condition in this disease and prolong the time of ambulation. However, corticosteroids also have the adverse consequence of increasing SF thickness, as they are strongly catabolic in nature. Thus, although muscle health improves, SF thickness increases and thus sEIM data suggests exacerbating disease since the impact of the SF thickness on the collected data increases (i.e., increasing fat in muscle suggests worsening disease). As a result, recent sEIM studies have led to relatively substantial overlap between healthy and diseased sEIM data due to the variability of SF tissue [36], [37].

The only previous work the authors are aware of in which SS methods are applied to the impedance field was to filter the cardiac and respiratory signals over time in electrical impedance

tomography [38], [39]. Here, instead, we consider the time-*in*variant dynamics of the impedivity of biological tissues as signals. These signals are mixed according to (7) in sEIM data where the frequency measured is now the independent variable. Drawing an analogy with the case of filtering signals in time domain, we use MCA to filter SF contribution to the impedance as a function of the frequency measured.

A feature of MCA –and SS methods in general– is that the frequency-dependence of the impedivity of SF and muscle tissues are estimated up to scaling of their true (unknown) amplitude values, i.e., the former is dimensionless whereas the latter has unit of Ω m. Still, MCA can be employed to improve the sensitivity of sEIM to detect diseased muscle and status calculating ratiometric indices at different frequencies. In fact, this is the existing approach that has been used to mitigate the impact of SF in sEIM values, e.g., calculating ratios 50/100 kHz [13], 50/200 kHz [12] or 100/300 kHz [14]. The difference between these approaches and our work is, however, with MCA it is possible to perform a meaningful ratiometric analysis using muscle impedivity data only.

There are a variety of limitations affecting this study. One of them is the Fricke-Morse model used, which describes the dynamics of biological tissues using three parameters only. Although the simulation results demonstrate the feasibility of modeling experimental muscle impedivity data with an averaged similarity being of 99.2%, it may even be possible to improve upon this by increasing the complexity of the model, for example, using the four-parameter Cole impedance model [40]. On the other hand, part of the 0.8% discrepancy between MCA and the reference simulation data may have originated from the technical difficulty of accurately measuring the impedivity of tissues. It is known that existing methods for measuring in situ the impedivity of anisotropic biologic tissues such as muscle have practical limitations [41]–[43]. Another limitation affecting our experimental results is the simplification of the domain studied here, where the contribution of the skin to the sEIM data is neglected. On top of that, the experimental data are also limited by the fact that the equivalent electrical circuit employed did not include possible measurement errors affecting the measured bioimpedance. Finally, to derive the linear system, we assumed that the sensitivity was constant and yet it depends on the domain, the electrodes' characteristics, the frequency measured, and the (unknown) tissues' impedivity values that we aim to be measure. Further work is required to increase the complexity of the analysis presented to address these limitations. In future work, we also plan to compare the estimated muscle impedivity using MCA with the impedivity measured ex vivo in patients undergoing muscle biopsy.

VIII. Conclusion

This paper presents model component analysis (MCA), a new nonblinded source separation method for separating the contribution of subcutaneous fat (SF) tissue affecting surface electrical impedance myography (sEIM) data using Fricke-Morse model. MCA allows the biomedical researcher or physician to evaluate with confidence the alterations to muscle tissue over time and the impact of therapy. The validity of the MCA method has been tested against standard source separation techniques including independent component analysis and principal component analysis through simulations and measurements on patients. Of the three methods studied, MCA's ability to remove the contribution of the confounding SF tissue and evaluate the actual change in muscle tissue only only as a function of disease progression or response to therapy has important clinical implications. First, it will make sEIM a more robust diagnostic tool capable of avoiding the signal artifacts introduced by SF tissue. In addition, it will simplify the clinical application of sEIM in longitudinal studies where changes of SF thickness reduce the sensitivity to detect disease progression and therapeutic effect.

Conflict of Interest

Dr. Rutkove has equity in, and serves as a consultant and scientific advisor to Myolex, Inc., a company that designs impedance devices for clinical and research use; he is also a member of the company's Board of Directors. The company also has an option to license patented impedance technology of which Dr. Rutkove is named as an inventor. Dr. Sanchez is named as an inventor on a patent application in the field of electrical impedance. Dr. Sanchez serves as a consultant to Maxim Integrated, Inc., and Impedimed, Inc., two companies that develop impedance devices for consumer electronics, clinical and research use. This study, however, did not employ any relevant company or patented technology.

References

[1] S. Grimnes and O. G. Martinsen, *Bioimpedance and Bioelectricity Basics*, 3rd ed. New York, NY, USA: Academic, 2014.
[2] B. Sanchez and S. B. Rutkove, "Electrical impedance myography and its applications in neuromuscular disorders," *Neurotherapeutics*, vol. 14, no. 1, pp. 107–118, Jan. 2017.
[3] S. B. Rutkove *et al.*, "Electrical impedance myography as a biomarker to assess ALS progression," *Amyotroph. lateral Scler.*, vol. 13, no. 5, pp. 439–445, Sep. 2012.
[4] B. Sanchez *et al.*, "Impedance alterations in healthy and diseased mice during electrically-induced muscle contraction," *IEEE Trans. Biomed. Eng.*, vol. 63, no. 8, pp. 1602–1612, Apr. 2014.
[5] J. Li *et al.*, "Electrical impedance myography for the in vivo and ex vivo assessment of muscular dystrophy (MDX) mouse muscle," *Muscle Nerve*, vol. 49, no. 6, pp. 829–835, Jun. 2014.
[6] B. Sanchez *et al.*, "Evaluation of electrical impedance as a biomarker of myostatin inhibition in wild type and muscular dystrophy mice," *PLoS One*, vol. 10, no. 10, Jan. 2015, Art. no. e0140521.
[7] A. W. Tarulli *et al.*, "Electrical impedance myography in the assessment of disuse atrophy," *Arch. Phys. Med. Rehabil.*, vol. 90, no. 10, pp. 1806–10, Oct. 2009.
[8] L. P. Garmirian *et al.*, "Discriminating neurogenic from myopathic disease via measurement of muscle anisotropy," *Muscle Nerve*, vol. 39, no. 1, pp. 16–24, Jan. 2009.
[9] L. L. Wang *et al.*, "Electrical impedance myography for monitoring motor neuron loss in the SOD1 G93A amyotrophic lateral sclerosis rat," *Clin. Neurophysiol.*, vol. 122, no. 12, pp. 2505–2511, Dec. 2011.
[10] L. Nescolarde *et al.*, "Localized bioimpedance to assess muscle injury," *Physiol. Meas.*, vol. 34, no. 2, pp. 237–245, Feb. 2013.
[11] S. B. Rutkove *et al.*, "Sensitivity distribution simulations of surface electrode configurations for electrical impedance myography," *Muscle Nerve*, vol. 56, no. 5, pp. 887–895, Jan. 2017.
[12] S. Schwartz *et al.*, "Optimizing electrical impedance myography measurements by using a multifrequency ratio: A study in Duchenne muscular dystrophy," *Clin. Neurophysiol.*, vol. 126, no. 1, pp. 202–208, 2015.

[13] L. Li *et al.*, "The effect of subcutaneous fat on electrical impedance myography: Electrode configuration and multi-frequency analyses," *PLoS One*, vol. 11, no. 5, Jan. 2016, Art. no. e0156154.
[14] S. B. Rutkove *et al.*, "Electrical impedance myography for assessment of Duchenne muscular dystrophy," *Ann. Neurol.*, vol. 81, no. 5, pp. 622–632, May 2017.
[15] R. Martin-Clemente and V. Zarzoso, "On the link between L1-PCA and ICA," *IEEE Trans. Pattern Anal. Mach. Intell.*, vol. 39, no. 3, pp. 515–528, Mar. 2017.
[16] M. S. Kang *et al.*, "ISAR cross-range scaling using iterative processing via principal component analysis and bisection algorithm," *IEEE Trans. Signal Process.*, vol. 64, no. 15, pp. 3909–3918, Aug. 2016.
[17] Y. Li *et al.*, "Underdetermined blind source separation based on sparse representation," *IEEE Trans. Signal Process.*, vol. 54, no. 2, pp. 423–437, Feb. 2006.
[18] E. C. Cherry, "Some experiments on the recognition of speech, with one and with two ears," *J. Acoust. Soc. Amer.*, vol. 25, no. 5, pp. 975–979, Sep. 1953.
[19] P. Comon, "Independent component analysis, A new concept?" *Signal Process.*, vol. 36, no. 3, pp. 287–314, Apr. 1994.
[20] A. Hyvärinen and E. Oja, "Independent component analysis: Algorithms and applications," *Neural Netw.*, vol. 13, pp. 411–430, 2000.
[21] A. Hyvarinen, "Fast and robust fixed-point algorithm for independent component analysis," *IEEE Trans. Neural Netw. Learn. Syst.*, vol. 10, no. 3, pp. 626–634, May 1999.
[22] M. C. Jones and R. Sibson, "What is Projection Pursuit?" *J. R. Stat. Soc. Ser. A*, vol. 150, no. 1, pp. 1–37, 1987.
[23] E. Somersalo *et al.*, "Existence and uniqueness for electrode models for electric current computed tomography," *SIAM J. Appl. Math.*, vol. 52, no. 4, pp. 1023–1040, 1992.
[24] D. B. Geselowitz, "An application of electrocardiographic lead theory to impedance plethysmography," *IEEE Trans. Biomed. Eng.*, vol. BME-18, no. 1, pp. 38–41, Jan. 1971.
[25] K. R. Foster and H. P. Schwan, "Dielectric properties of tissues and biological materials: A critical review," *Crit. Rev. Biomed. Eng.*, vol. 17, no. 1, pp. 25–104, 1989.
[26] H. Kwon *et al.*, "New electrical impedance methods for the in situ measurement of the complex permittivity of anisotropic biological tissues," *Phys. Med. Biol.*, vol. 62, no. 22, pp. 8616–8633, Sep. 2017.
[27] S. Rush, "Methods of measuring the resistivities of anisotropic conducting media in situ," *J. Res. Nat. Bur. Stand. Sect. C Eng. Instrum.*, vol. 66C, no. 3, p. 217, 1962.
[28] H. Fricke and S. Morse, "The electric resistance and capacity of blood for frequencies between 800 and 4(1/2) million cycles," *J. Gen. Physiol.*, vol. 9, no. 2, pp. 153–167, Nov. 1925.
[29] B. Sanchez *et al.*, "On the calculation of the D-optimal multisine excitation power spectrum for broadband impedance spectroscopy measurements," *Meas. Sci. Technol.*, vol. 23, no. 23, Oct. 2012, Art. no. 085702.
[30] B. Sanchez *et al.*, "Novel approach of processing electrical bioimpedance data using differential impedance analysis," *Med. Eng. Phys.*, vol. 35, no. 9, pp. 1349–1357, Sep. 2013.
[31] B. Sanchez and C. R. Rojas, "Robust excitation power spectrum design for broadband impedance spectroscopy," *Meas. Sci. Technol.*, vol. 25, no. 6, 2014, Art. no. 065501.
[32] E. Louarroudi and B. Sanchez, "On the correct use of stepped-sine excitations for the measurement of time-varying bioimpedance," *Physiol. Meas.*, vol. 38, no. 2, pp. N73–N80, Dec. 2017.
[33] D. Andreuccetti *et al.*, "An Internet resource for the calculation of the dielectric properties of body tissues in the frequency range 10 Hz–100 GHz," *Neuromuscular Disorders*, vol. 22, no. 4, pp. 306–317, Apr. 2012.
[34] M. Jansen *et al.*, "Quantitative muscle ultrasound is a promising longitudinal follow-up tool in Duchenne muscular dystrophy," *Neuromuscul. Disord.*, vol. 22, no. 4, pp. 306–317, Apr. 2012.
[35] H. P. Schwan, "Electrical and acoustic properties of biological materials and biomedical applications," *IEEE Trans. Biomed. Eng.*, vol. BME-31, no. 12, pp. 872–878, Dec. 1984.
[36] S. B. Rutkove *et al.*, "Cross-sectional evaluation of electrical impedance myography and quantitative ultrasound for the assessment of Duchenne muscular dystrophy in a clinical trial setting," *Pediatr. Neurol.*, vol. 51, no. 1, pp. 88–92, Jul. 2014.
[37] S. B. Rutkove *et al.*, "Characterizing spinal muscular atrophy with electrical impedance myography," *Muscle Nerve*, vol. 42, no. 6, pp. 915–921, Dec. 2010.
[38] J. M. Deibele *et al.*, "Dynamic separation of pulmonary and cardiac changes in electrical impedance tomography," *Physiol. Meas.*, vol. 29, no. 6, pp. S1–S14, Jun. 2008.
[39] T. Rahman *et al.*, "Extraction of cardiac and respiration signals in electrical impedance tomography based on independent component analysis," *J. Elect. Bioimpedance*, vol. 4, no. 1, pp. 38–44, Oct. 2013.
[40] K. S. Cole, "Permeability and impermeability of cell membranes for ions," *Cold Spring Harbor Symp. Quant. Biol.*, vol. 8, pp. 110–122, Jan. 1940.
[41] Y. Wang *et al.*, "Geometric effects on resistivity measurements with four-electrode probes in isotropic and anisotropic tissues," *IEEE Trans. Biomed. Eng.*, vol. 45, no. 7, pp. 877–884, Jul. 1998.
[42] S. Kun and R. Peura, "Effects of sample geometry and electrode configuration on measured electrical resistivity of skeletal muscle," *IEEE Trans. Biomed. Eng.*, vol. 47, no. 2, pp. 163–169, Feb. 2000.
[43] J. Z. Tsai *et al.*, "Dependence of apparent resistance of four-electrode probes on insertion depth," *IEEE Trans. Biomed. Eng.*, vol. 47, no. 1, pp. 41–48, Jan. 2000.